

Three-dimensional Analytical Description of Magnetised Winds from Oblique Pulsars

Alexander Tchekhovskoy^{1,2*}†, Alexander Philippov³ and Anatoly Spitkovsky³

¹*Department of Astronomy, University of California Berkeley, Berkeley, CA 94720-3411*

²*Lawrence Berkeley National Laboratory, 1 Cyclotron Rd, Berkeley, CA 94720, USA*

³*Department of Astrophysical Sciences, Peyton Hall, Princeton University, Princeton, NJ 08544, USA*

Accepted . Received ; in original form

ABSTRACT

Rotating neutron stars, or pulsars, are plausibly the source of power behind many astrophysical systems, such as gamma-ray bursts, supernovae, pulsar wind nebulae and supernova remnants. In the past several years, 3D numerical simulations made it possible to compute pulsar spindown luminosity from first principles and revealed that oblique pulsar winds are more powerful than aligned ones. However, what causes this enhanced power output of oblique pulsars is not understood. In this work, using time-dependent 3D magnetohydrodynamic (MHD) and force-free simulations, we show that, contrary to the standard paradigm, the open magnetic flux, which carries the energy away from the pulsar, is laterally non-uniform. We argue that this non-uniformity is the primary reason for the increased luminosity of oblique pulsars. To demonstrate this, we construct simple analytic descriptions of aligned and orthogonal pulsar winds and combine them to obtain an accurate 3D description of the pulsar wind for any obliquity. Our approach describes both the warped magnetospheric current sheet and the smooth variation of pulsar wind properties outside of it. We find that generically the magnetospheric current sheet separates plasmas that move at mildly relativistic velocities relative to each other. This suggests that the magnetospheric reconnection is a type of driven, rather than free, reconnection. The jump in magnetic field components across the current sheet decreases with increasing obliquity, which could be a mechanism that reduces dissipation in near-orthogonal pulsars. Our analytical description of the pulsar wind can be used for constructing models of pulsar gamma-ray emission, pulsar wind nebulae, and magnetar-powered core-collapse gamma-ray bursts and supernovae.

Key words: pulsars: general – stars: neutron – stars: rotation – stars: magnetic field.

1 INTRODUCTION

A rotating magnet in vacuum is the simplest description of a rotating neutron star, or pulsar. The magnet loses its energy to magnetodipole radiation (Deutsch 1955). However, real pulsar magnetospheres are likely filled with plasma (Goldreich & Julian 1969), which supports charges and currents that modify the pulsar spindown. For a long time it has been realized that plasma-filled magnetospheres open up to infinity due to relativistic rotation (Ingraham 1973; Michel 1974). The open magnetic flux carries away the spindown luminosity of the star in the form of a pulsar wind.

Whereas the origin of spindown luminosity of vacuum rotators has been well-understood due to the availability of the analytic model, the spindown of plasma-filled magnetospheres can only be studied numerically, and progress became possible only recently.

The primary difficulty in computing pulsar magnetosphere structure is in connecting the conditions on the star to the properties of the emerging pulsar wind. Of particular importance is the determination of the twist of magnetic field lines at the stellar surface, or the magnitude of the electric current flowing through the magnetosphere. Early pulsar magnetosphere solutions prescribed the magnitude of the twist, and, as a result, the solutions extended smoothly only to the *light cylinder* radius (Beskin, Gurevich & Istomin 1993; Mestel & Shibata 1994; Beskin 1997), the distance from the rotational axis at which a field line rigidly rotating at the frequency of the central object would move at the speed of light,

$$R_{\text{LC}} = \frac{c}{\Omega}, \quad (1)$$

where $\Omega = 2\pi/P$ is pulsar angular frequency and P is the period.

In real magnetospheres, the magnitude of the magnetospheric current is set self-consistently by the large-scale properties of the magnetosphere. The rotation of the star twists the magnetic field lines, which sends out a torsional Alfvén wave that carries the twist outward. On the way out, the Alfvén wave undergoes partial re-

* Einstein Fellow

† Email: atchekho@berkeley.edu, philippo@astro.princeton.edu, anatoly@astro.princeton.edu

flections that reach back to the star and modify the surface value of the magnetic field twist, which determines the strength of the magnetospheric current. It is accounting for this communication by Alfvén waves and determining the correct value of the magnetospheric current that was the challenge. Contopoulos, Kazanas & Fendt (1999) found an iterative way to determine the strength of the magnetospheric current self-consistently. They obtained the first solution for an *aligned* force-free pulsar magnetosphere that extended out to infinity. Their results were subsequently verified by other groups within force-free and magnetohydrodynamic (MHD) approximations (e.g., Gruzinov 2005; Timokhin 2006; McKinney 2006; Komissarov 2006; Parfrey, Beloborodov & Hui 2012; Ruiz, Paschalidis & Shapiro 2014) as well as using a particle-in-cell (PIC) approach (Philippov & Spitkovsky 2014; Chen & Beloborodov 2014; Cerutti, Philippov, Parfrey & Spitkovsky 2014; Belyaev 2014).

Spitkovsky (2006) carried out the first 3D, oblique pulsar magnetosphere simulations. Using the force-free approximation, he found that pulsar spindown luminosity increases with increasing obliquity angle, α , the angle between the rotational and magnetic axes. More recently, these results were confirmed using time-dependent 3D force-free (Kalapotharakos & Contopoulos 2009; Pétri 2012; Kalapotharakos, Contopoulos & Kazanas 2012), MHD (Tchekhovskoy, Spitkovsky & Li 2013), and PIC (Philippov, Spitkovsky & Cerutti 2014) studies.

Despite these advances, what sets the spindown luminosity of plasma-filled pulsars remains elusive. Understanding this and constructing a detailed, 3D model of a pulsar wind are the goals of this work. We start with a discussion of pulsar spindown in the split-monopole approximation and confront it with the numerical simulations in §2, discuss the effects of pulsar wind non-uniformity on pulsar spindown rate and develop a toy model of a non-uniform pulsar wind in §3. We construct an analytic description of aligned and orthogonal plasma-filled pulsar winds in §4. We then try and get an inspiration on how to construct solutions for intermediate inclination angles in §5 and construct our analytical description of the pulsar wind for an arbitrary inclination angle in §6. We discuss our results and their observational implications in §7. We will use spherical polar coordinates, (r, θ, φ) , cylindrical coordinates, (R, z, φ) , and Cartesian coordinates, (x, y, z) .

2 DEPENDENCE OF SPIN-DOWN POWER ON INCLINATION AND THE STRUCTURE OF PULSAR WIND

Our goal is to understand the physics of spindown of plasma-filled pulsars. The solid blue line in Fig. 1 shows the dependence of pulsar spindown on inclination (see Spitkovsky 2006; Pétri 2012; Tchekhovskoy et al. 2013; Philippov et al. 2014). Clearly, oblique pulsars have higher spindown rates, but the reason for this increase is unclear. In the widely used and highly successful standard model of the asymptotic pulsar wind, the wind structure is radial and is that of a split-monopole outflow (Bogovalov 1999). The wind indeed appears to be radial far from the pulsar, as is seen in Fig. 2. However, this brings up a problem: the spindown of split-monopole solution is *independent* of inclination! In it, $|r^2 B^r| = \text{constant}$ and is time-independent. In fact, as we will derive below (see eq. 14), the spindown luminosity is set by the rotational frequency of the star, $\Omega_* = 2\pi/P$, and the amount of open magnetic flux in the split-

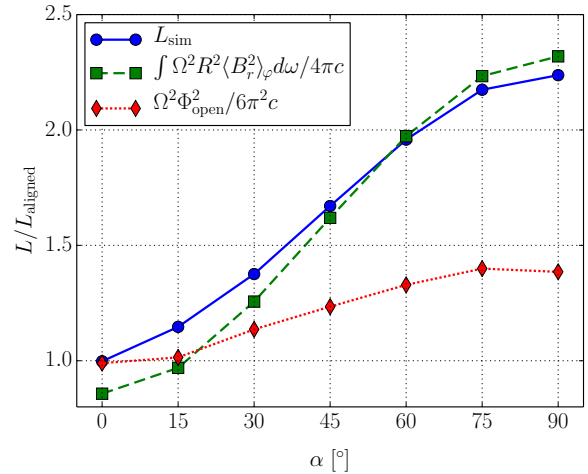


Figure 1. Blue solid line shows the dependence of spindown luminosity on the inclination angle, α , in a series of MHD simulations (Tchekhovskoy et al. 2013). Red dotted line shows the corresponding spindown luminosity for a split-monopole wind (same open magnetic flux as in the simulation). It accounts for about 40% of the increase but falls short of explaining the full magnitude of the increase in luminosity with increasing α . Green dashed line shows the spindown for a non-uniform distribution of open magnetic flux (same non-uniformity as in the simulation). It matches the simulated luminosity well. The non-uniformity of the open magnetic flux plays a crucial role in setting the spindown luminosity of oblique pulsars.

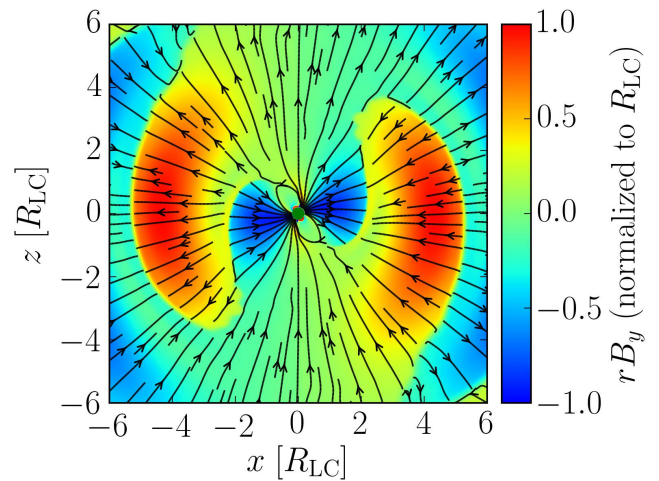


Figure 2. Magnetic field structure of pulsar wind in the $\vec{\mu}-\vec{\Omega}$ plane of an oblique, $\alpha = 60^\circ$, MHD simulation. Solid black lines show magnetic field lines and color shows rB_y , into-the-plane magnetic field component (which we rescaled by the r prefactor to remove the trivial radial trend). That the magnetic field lines are predominantly straight suggests that the magnetospheric outflow is nearly radial. However, as indicated by non-trivial variations of rB_y , whose absolute magnitude would be a constant along $\theta = \text{constant}$ in a split-monopole solution, this does not mean that the solution is well-described by a split-monopole (see also Fig. 4).

monopole solution,

$$\Phi_{\text{open}} = (1/2) \iint |B_r| d\omega, \quad (2)$$

where the integral is over both hemispheres and the factor of (1/2) converts it to a single hemisphere. For a split-monopole magnetic field, eq. (2) reduces to $\Phi_{\text{open}} = 2\pi r^2 |B_r|$, and the spindown lumi-

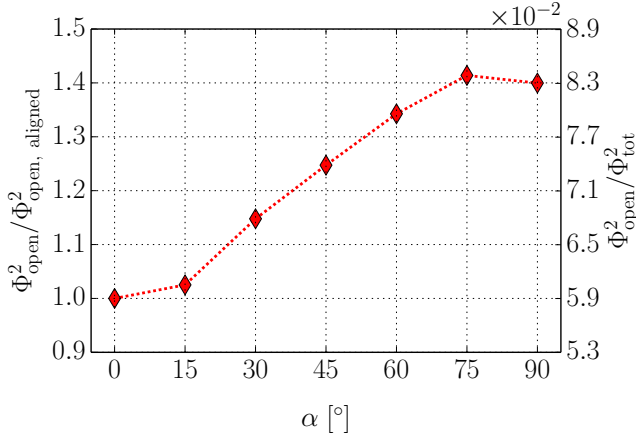


Figure 3. The square of the open magnetic flux Φ_{open} measured according to eq. (2) at a sphere of radius $r = 2R_{\text{LC}}$, plotted versus the inclination angle, α , in a series of MHD simulations. The open magnetic flux increases with increasing inclination angle. This increase accounts for $\approx 40\%$ of the enhancement in spindown luminosity of oblique rotators. The remaining 60% come from the redistribution of the open magnetic flux toward the equatorial plane (see §3).

nosity is

$$L = \frac{\Omega^2 \Phi_{\text{open}}^2}{6\pi^2 c}, \quad (\text{uniform } |r^2 B_r|) \quad (3)$$

where c is the speed of light.

A natural possibility is that the amount of open magnetic flux depends on the inclination angle, $\Phi_{\text{open}} = \Phi_{\text{open}}(\alpha)$, and this causes the dependence of the spindown luminosity on α . Fig. 3 shows that while this is indeed the case to a degree, the dependence $\Phi_{\text{open}}(\alpha)$ is too weak to fully account for the enhancement in spindown rate for oblique pulsars. In fact, it accounts for about 40% of the luminosity enhancement, as shown with red dotted lines in Figs. 1 and 3. What is the cause of the rest of the enhancement, i.e., the difference between the dotted red and solid blue lines?

3 NON-UNIFORMITY OF ASYMPTOTIC PULSAR WIND AND SPINDOWN RATE

As the colour variation in Fig. 4 suggests, the product $|r^2 B_r|$ is not constant in the simulated pulsar wind. However, the split-monopole model of the pulsar wind and the associated spindown luminosity given by equation (3) assume that $|r^2 B_r|$ is a constant everywhere, i.e., apart from B_r changing sign at current sheet crossings, B_r is laterally-uniform (i.e., it has no dependence on θ and φ) and follows a simple power-law dependence in radius. According to Fig. 4, this approximation is at best very rough: B_r shows variations away from the expected scaling, $1/r^2$, which indicates the presence of a substantial, order unity non-uniformity in the pulsar wind. Can these non-uniformities lead to deviations from the spindown rate given by equation (3)? In section §3.1 we will demonstrate that this is indeed the case.

3.1 Velocity and freeze-in condition in ideal MHD

To describe the asymptotic structure of pulsar wind, we will make use of the fact that the wind structure is accurately described by a 2D distribution of just a single variable, B_r , in θ - φ plane. This

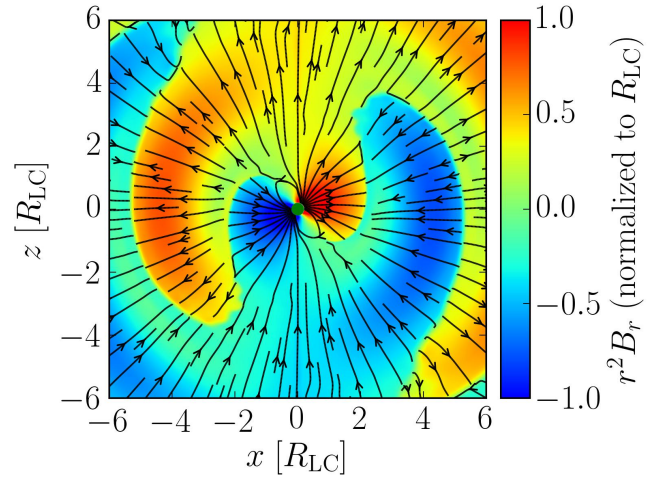


Figure 4. The same magnetospheric structure as Fig. 2 but with colour showing scaled radial magnetic field, $r^2 B_r$. The r^2 -prefactor eliminates the obvious radial trend: for a perfectly monopolar field, we would have $r^2 B_r = \text{const}$. The substantial deviations from constancy of $r^2 B_r$ are a strong indication that the radial magnetic field in the pulsar magnetosphere is substantially non-uniform and deviates from the simple monopolar dependence, $B_r \propto 1/r^2$.

can be seen as follows. In ideal MHD/force-free a pulsar magnetosphere rotates at the stellar angular frequency. Thus, the velocity can be decomposed into motion along magnetic field lines with velocity v_{\parallel} and together with the magnetic field lines corotating with the star at $v_{\varphi} = \Omega r \sin \theta$:

$$\vec{v} = v_{\parallel} \frac{\vec{B}}{|\vec{B}|} + \Omega r \sin \theta \vec{e}_{\varphi}. \quad (4)$$

Due to the ideal MHD condition, the electric field is $\vec{E} = -(\vec{v}/c) \times \vec{B} = -(\Omega r \sin \theta/c) B_r \vec{e}_{\theta}$.

Asymptotically far from the pulsar, $r \sin \theta \gg R_{\text{LC}}$, the magnetic field is toroidally-dominated, $B_{\varphi} \gg B_r, B_{\theta}$ and moves outward at a drift velocity,

$$v_{\text{dr}} = \frac{c|\vec{E} \times \vec{B}|}{B^2} \approx \frac{cE_{\theta} B_{\varphi}}{B_{\varphi}^2}. \quad (5)$$

Since at such large distances the wind moves relativistically fast, $v_{\text{dr}} \approx c$, we have:

$$B_{\varphi} \approx -E_{\theta} = -(\Omega r \sin \theta/c) B_r. \quad (6)$$

Using eq. (6), for a given distribution of B_r , we can reconstruct the rest of the field components.

3.2 Poynting flux

Using eq. (6), we can write the Poynting flux, which is carried by the outflowing toroidal magnetic field, as

$$S_r = \frac{c}{4\pi} (\vec{E} \times \vec{B})_r \approx \frac{\Omega^2}{4\pi c} B_r^2 r^2 \sin^2 \theta. \quad (7)$$

Thus, the spindown luminosity is given by

$$L = \iint S_r d\omega = 2\pi \int_0^{\pi} \langle S_r \rangle_{\varphi} r^2 \sin \theta d\theta \approx \frac{\Omega^2}{2c} \int_0^{\pi} \langle B_r^2 \rangle_{\varphi} r^4 \sin^3 \theta d\theta, \quad (8)$$

where $\langle \dots \rangle_\varphi$ is the averaging over φ , and we used the expression for the φ -average Poynting flux,

$$\langle S_r \rangle_\varphi \equiv \left\langle \frac{\partial L}{\partial \omega} \right\rangle_\varphi = \frac{\Omega^2}{4\pi c} \langle B_r^2 \rangle_\varphi r^2 \sin^2 \theta, \quad (9)$$

that trivially follows from the definition of S_r , eq. (7). Both L and its angular distribution $\langle \partial L / \partial \omega \rangle_\varphi$ are fully determined by the surface distribution of a single quantity, $B_r(\theta, \varphi)$, or, more precisely, by the φ -average of its square, $\langle B_r^2 \rangle_\varphi$.

If the magnetic field is split-monopolar, i.e., $|B_r| = B_0(r_0/r)^2$ and $B_0 = \Phi_{\text{open}}/2\pi r_0^2$, eq. (8) reduces to the standard split-monopolar expression, eq. (3). Note, however, that the real pulsar wind is non-uniform laterally, and this approximation does not capture this nonuniformity. However, even despite the non-uniformity, the pulsar wind remains very nearly radial. This means that the radial scaling of B_r is a trivial power-law, $\propto r^{-2}$.

3.3 Dipolar approximation for radial magnetic field

To make progress, we will approximate the angular distribution of B_r in the open magnetic flux region by that of a dipole $\vec{\mu}$ inclined at an angle α in the x - z , or $\varphi = 0$, plane. As we will see below, this is an excellent approximation for near-orthogonal rotators and a reasonable approximation for other obliquities. We obtain:

$$B_r = B_0(r/r_0)^{-2} \cos \theta_m, \quad (10)$$

where θ_m is magnetic colatitude, the angle away from the magnetic axis,

$$\theta_m = \arccos(\sin \alpha \sin \theta \cos \varphi + \cos \theta \cos \alpha), \quad (11)$$

and

$$B_0 = \Phi_{\text{open}}/\pi r_0^2. \quad (12)$$

The angular distribution of B_r due to eq. (10) is clearly nonuniform: B_r is strongest at the magnetic poles ($\cos \theta_m = \pm 1$) and weakest along the magnetic equator ($\cos \theta_m = 0$).

To find out how this nonuniformity affects the spindown, we first compute the angular distribution of φ -averaged B_r^2 :

$$\langle B_r^2 \rangle_\varphi = B_0^2(r/r_0)^{-4} (0.5 \sin^2 \alpha \sin^2 \theta + \cos^2 \theta \cos^2 \alpha). \quad (13)$$

Now, by plugging eq. (13) into eq. (8) and integrating, we obtain:¹

$$L_{\text{dipole}}(\alpha) = \frac{\Omega^2 \Phi_{\text{open}}^2}{7.5\pi^2 c} (1 + \sin^2 \alpha). \quad (14)$$

This is very close to the α -dependence that is observed in numerical simulations and shown in Fig. 1 with the solid blue line. Therefore, the nonuniformity of B_r , via the magnetic flux concentration toward the magnetic poles (i.e., around the direction of $\vec{\mu}$), causes an *enhancement in spindown losses* at high inclination angles ($\alpha \sim 90^\circ$).

The qualitative behaviour given by eq. (14) has a clear physical interpretation. From eq. (7) we see that energy flux is minimum near the rotational poles ($\sin \theta \approx 0$) and maximum near the rotational equator ($\sin \theta \approx 1$). Hence, the spindown losses are minimised when the maximum in B_r is along the rotational poles and does not contribute to the spindown ($\alpha = 0$). Conversely, the spindown losses are maximised when the maximum in B_r lies in the rotational equator and contributes to the spindown most efficiently

¹ Note that since in a dipole the open magnetic field depends on the pulsar period, $\Phi_{\text{open}} \propto \Omega$, the dependence on the period is in 4th power, $L_{\text{dipole}} \propto \Omega^4$.

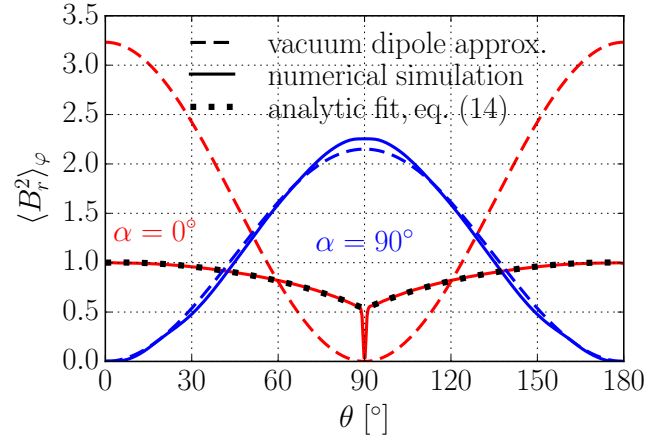


Figure 5. The lateral distribution of azimuthally-averaged B_r^2 (which determines the spindown rate, see eq. 8) due to (i) numerical simulation shown with solid curves and due to (ii) the B_r distribution for vacuum dipole, eq. (10), with dashed curves. Red lines show the results for the aligned and solid lines for the orthogonal rotator. Both distributions are normalised to have the same magnetic flux. The vacuum dipole approximation accurately reproduces the lateral distribution of magnetic field for the orthogonal rotator, as shown with red curves. However, it substantially over-predicts the polar field strength and under-predicts the equatorial field strength for the aligned rotator. The dotted black line shows an analytic fit (18) for the force-free aligned rotator simulation results.

($\alpha = 90^\circ$). In other words, the spindown losses are higher than in a pure monopole because of angular redistribution of magnetic flux from the polar to the equatorial regions.

From eqs. (10) and (11), the radial magnetic field strength of an orthogonal rotator is:²

$$B_r^{(2)}(r, \theta, \varphi) = B_0(r/r_0)^{-2} \sin \theta \cos \varphi. \quad (\text{for orthogonal pulsars}) \quad (15)$$

The azimuthally-average of (15) is highly non-uniform laterally (see also eq. 13):

$$\langle B_r^2 \rangle_\varphi = 0.5 B_0^2(r/r_0)^{-4} \sin^2 \theta. \quad (16)$$

This nonuniformity implies that the angular distribution of spindown luminosity deviates from the standard expectation, $dL/d\omega \propto \sin^2 \theta$, eq. (9), and becomes,

$$\left\langle \frac{\partial L_{90}}{\partial \omega} \right\rangle_\varphi = \frac{\Omega^2 \Phi_{\text{open}}^2}{8\pi^3 c r^2} \sin^4 \theta, \quad (\text{for orthogonal pulsars}) \quad (17)$$

where we used the eq. (12) to eliminate B_0 in favour of Φ_{open} .

4 APPROXIMATE SOLUTION FOR ALIGNED AND ORTHOGONAL FORCE-FREE PULSAR WINDS

In Section 3.3, we found that magnetic field line bunching around the magnetic poles, such as in a vacuum dipole, qualitatively reproduces the increased spindown rate of oblique force-free and MHD pulsars. This is because most of the spindown emanates near the equatorial plane, $\theta = \pi/2$, as indicated by the factor $\sin^3 \theta$ in eqs. (8) and (9). Thus, for a field line to contribute to spindown most efficiently, it needs to be close to the equatorial plane. As we tilt the

² This also coincides with B_r distribution of the full vacuum solution (Deutsch 1955).

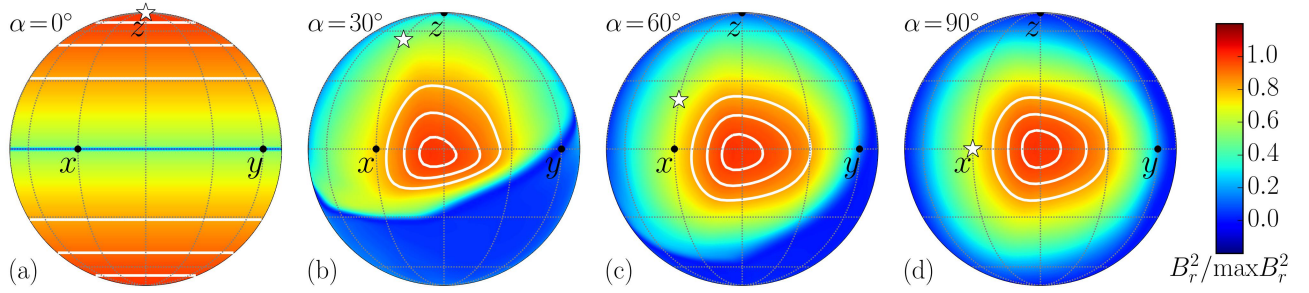


Figure 6. Colour-coded surface distribution of B_r^2 in the numerical force-free solution (red shows high blue low values, see colour bar) for different inclination angles, at the surface of a sphere of radius $r = 6R_{\text{LC}}$. The white contours indicate 91st, 96th, and 99th percentile levels of B_r , which was Gaussian-smoothed with a standard deviation of 1.5 cells. At all inclination angles the angular distribution of B_r^2 is clearly non-uniform. Even though for an aligned rotator, shown in **panel (a)**, the maximum in B_r^2 follows the polar field line (shown with the white asterisk), for other inclination angles (**panels b-d**) the magnetic peak shifts: it moves laterally closer to equatorial plane and shifts in azimuth to a later phase by about $\varphi_{\text{max}} \approx 30^\circ$ (see also Fig. 7). Note that at nonzero inclination angles (**panels b-d**), the peak in the solution resembles that of the orthogonal rotator (**panel d**).

pulsar, its magnetic pole, which is the region of enhanced magnetic field, approaches the rotational equator. This leads to an enhancement in the spindown.

To find out whether this mechanism is at work in the simulated pulsar magnetospheres, we compare the angular distributions of B_r due to a vacuum dipole solution, given by eq. (10), and in a simulation of a force-free magnetosphere. Since we are interested in the spindown rate, we will start by looking at an azimuthal average, $\langle B_r^2 \rangle_\varphi$, which determines the spindown luminosity (see eq. 8).

Figure 5 shows the comparison of the vacuum dipole approximation given by eq. (10) and numerical force-free simulations for two limiting cases: aligned and orthogonal rotators. The vacuum dipole curves are normalised to have the same open magnetic flux as in the numerical simulation (at the same obliquity).

From Fig. 5, we see that the simulation result for the orthogonal rotator is well approximated by eq. (16). Thus, the vacuum dipole provides an excellent description of an orthogonal rotator wind. We adopt eq. (16) as the analytic description of the magnetosphere of an orthogonal plasma-filled rotator.

At the same time, Fig. 5 shows that the vacuum dipole expression gives a very poor description of the aligned rotator solution: whereas in the simulation B_r is non-zero in the equatorial region, in the vacuum dipole field B_r vanishes at the equator. Since the total magnetic flux is the same, the polar field strength in the vacuum model by a factor ≈ 3 exceeds that in the simulation.

For this reason, we adopt the following fit as the analytic approximation for the aligned force-free solution:

$$B_r^{(1)}(\theta) = B_0(r/r_0)^{-2} [1 + 0.02 \sin \theta + 0.22(\cos \theta - 1) - 0.07(\cos \theta - 1)^4] \times \text{sign} \cos \theta. \quad (18)$$

This fit, shown in Fig. 5 with the black dotted line, provides an adequate quantitative description of the aligned force-free solution (at a representative distance $r = 6R_{\text{LC}}$ by which the solution has approximately settled to an asymptotic distribution). We discuss the lateral structure of this distribution in Appendix A.

5 PULSAR WIND STRUCTURE IN MAGNETIC COORDINATES

In §3, we obtained analytic approximations, eqs. (15) and (18), for $B_r(\theta, \varphi)$ – and thus an approximate description of the pulsar wind – for the two limiting cases of aligned and orthogonal rotators. Our

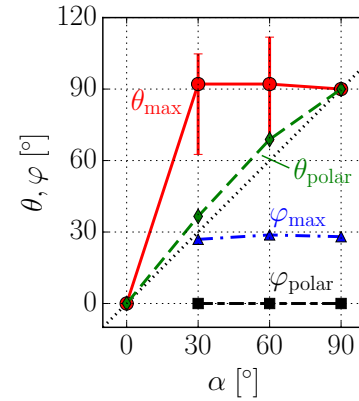


Figure 7. Positions of the polar field line and maximum in B_r are plotted with various lines vs the inclination angle, α , as measured at the sphere of radius $r = 6R_{\text{LC}}$. Shown are the polar coordinates of the maximum in magnetic field, $(\theta_{\text{max}}, \varphi_{\text{max}})$, with error bars indicating the range spanned by the outermost white contour in Fig. 6. We also plot the coordinates of the polar field line $(\theta_{\text{polar}}, \varphi_{\text{polar}})$, as labeled in the figure. The maximum of the field, shown with blue connected triangles, is located near the equatorial plane and outruns the polar field line by $\geq 30^\circ$ for $\alpha \sim 30\text{--}60^\circ$. The polar angle of the polar field line, which is shown with the green connected diamonds, approximately follows the inclination angle, i.e., the polar field line, despite being wrapped around in the azimuthal direction, maintains its polar angle. By definition we use the intersection point with the polar field line to set the zero point in the azimuth, i.e., we set $\varphi_{\text{polar}} = 0$.

goal is to obtain the description for pulsar wind at all inclination angles. Could we somehow combine these two expressions in order to get a general solution? With this in mind, let us look at the structure of the force-free pulsar winds simulations at various inclinations.

Fig. 6 shows the map of B_r^2 in the numerical force-free solution of a pulsar wind on the surface of a sphere of radius $r_0 = 6R_{\text{LC}}$. By this distance, the structure of the wind has frozen out and does not change at larger distances. Panels (a)–(d) illustrate solutions for different inclination angles, $\alpha = 0, 30, 60,$ and 90° , respectively, in two ways: (i) via a colour map (see the colour bar) and (ii) with white contours that indicate 91, 96, and 99 percentile levels of $\max |B_r|$.

For each inclination angle, B_r^2 exhibits a well-defined peak. The distribution of B_r for the aligned rotator, shown in Fig. 6(a), peaks at the rotational z -axis, as consistent with Fig. 5.

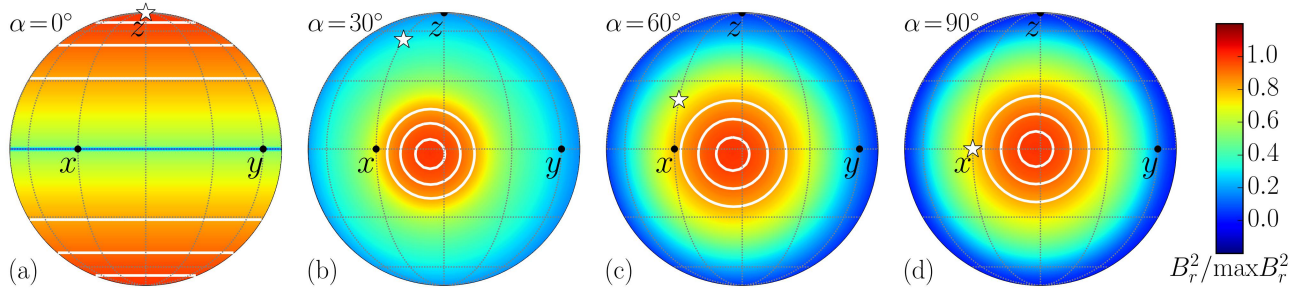


Figure 9. Colour-coded surface distribution of B_r^2 in the numerical force-free solution that was averaged out around the magnetic peak. For inclinations $\alpha \gtrsim 60^\circ$, this axial averaging approach gives a good approximation of solution structure around the peak. However, the averaging washes out the current sheet, which is a source of magnetospheric dissipation and potential origin of gamma-ray emission. See Fig. 6 for more details.

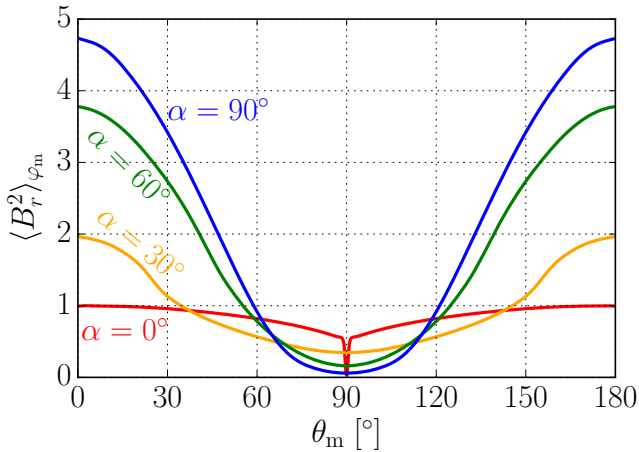


Figure 8. Angular distribution of the $\langle B_r^2 \rangle_{\varphi_m}$ of the numerical force-free solution in *magnetic coordinates* morphs from that of an aligned rotator at $\alpha = 0^\circ$ (red line) to that of an orthogonal rotator at $\alpha = 90^\circ$ (blue line). The in-between distributions, for intermediate inclination angles, $0^\circ < \alpha < 90^\circ$ resemble neither of these two limiting solutions, making it difficult to construct an analytic solution for those obliquities.

How does the situation change for an oblique rotator? We show the solution for a 30-degree inclined rotator in Fig. 6(b). The white star shows the point at which the polar field line pierces our sphere of $r = 6R_{LC}$. We denote this position as $(\theta_{\text{polar}}, \varphi_{\text{polar}})$ and use it to define the zero meridian, and with it our x - z plane. Thus, by definition we set $\varphi_{\text{polar}} = 0$. Figs. 6 and 7 show that θ_{polar} exceeds the inclination angle by only a few degrees: this means that as the polar field line propagates out and winds up around the rotational axis, it does so mostly along a cone of a constant opening angle.

However, this does not mean that the entire magnetosphere tilts rigidly and retains its lateral structure. If it did so, we would expect the peak in B_r to shift by the inclination angle, i.e. we would expect to have $\theta_{\text{max}} = \alpha$. Figures 6(b) and 7 show that this does not happen: for a stellar tilt of $\alpha = 30^\circ$, the peak tilts by three times as much, $\theta_{\text{max}} \approx 90^\circ$. Figs. 6(c) and 7 show that this trend persists for higher inclination angles: e.g., for $\alpha = 60^\circ$, we also find $\theta_{\text{max}} \approx 90^\circ$. The polar field line and the peak in B_r only catch up with each other for an orthogonal rotator, $\alpha = \theta_{\text{max}} = 90^\circ$. Therefore, a tilted magnetosphere rearranges itself in a non-trivial way, with different parts moving relative to each other and causing the maximum of radial magnetic field strength to shift toward the equatorial plane by more than we would naively expect.

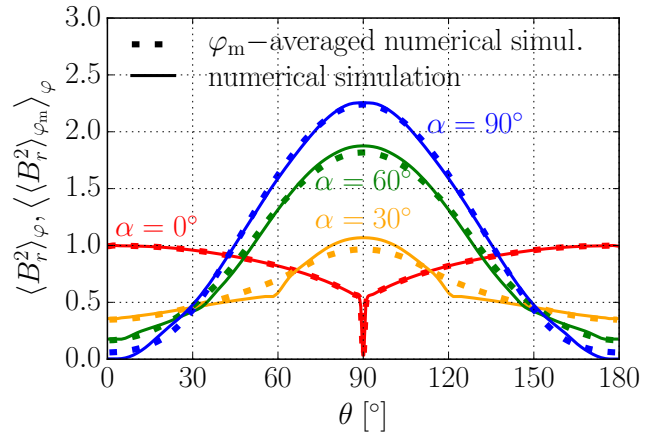


Figure 10. Angular distribution of the $\langle B_r^2 \rangle_{\varphi}$ in force-free simulations (solid lines) and same numerical simulation result but additionally φ_m -averaged around the magnetic peak, $\langle \langle B_r^2 \rangle_{\varphi_m} \rangle_{\varphi}$ (dotted lines) for different obliquities. The angle-averaging around the magnetic pole gives a good approximation for $\alpha = 0^\circ$ and $\alpha \gtrsim 60^\circ$ but washes out the non-axisymmetric structure around the pole at intermediate inclinations, which manifests itself as the smoothing out of the equatorial peak in the dotted orange $\langle \langle B_r^2 \rangle_{\varphi_m} \rangle_{\varphi}$ for $\alpha = 30^\circ$.

Note that the above picture applies at a rather large distance from the stellar surface, $r = 6R_{LC}$. At much smaller distances, e.g., at the surface of the star, the magnetic peak and the polar field line coincide. They smoothly diverge from each other with increasing distance from the stellar surface. The solution shown in Fig. 6 qualitatively persists out to much larger distances; asymptotically far away from the star, however, it undergoes small quantitative changes. We expect that at larger distances, $r > 6R_{LC}$, the solution does not have much opportunity to rearrange laterally: this is because the Lorentz factor of the wind scales as $\gamma \approx R/R_{LC} \gg 1$, and hence we expect that the solution might only be able to change on the small angular scales, $\delta\theta \sim 1/\gamma \sim R_{LC}/R \lesssim 1/6 \approx 10^\circ$ for $R > 6R_{LC}$.

Despite this magnetospheric rearrangement, the surface distribution of $B_r^2(r_0, \theta, \varphi)$ appears to maintain a rather high degree of symmetry around the magnetic peak, $(\theta_{\text{max}}, \varphi_{\text{max}})$. Are the deviations from axisymmetry around the peak important for the angular distribution of emergent luminosity? To test this, we plot in Fig. 8 the magnetic field distribution vs the magnetic co-latitude θ_m (which is counted off from the magnetic peak), averaged over the magnetic azimuth φ_m (relative to the magnetic peak), $\langle B_r^2 \rangle_{\varphi_m}$.

We see that as the inclination angle increases, the profile of $\langle B_r^2 \rangle_{\varphi_m}$ smoothly transitions from that of an aligned pulsar (red line, $\alpha = 0^\circ$) to that of a vacuum dipole, $B_r^2 \propto \cos^2 \theta_m$ (blue line, $\langle B_r^2 \rangle_{\varphi_m}$). This is another indication that the vacuum dipole magnetic field distribution provides a good description of the orthogonal pulsar.

Fig. 9 shows that after averaging out in φ_m , the solution visually appears very similar to the full force-free simulation. Will this approximation give a similar spindown compared to the simulation? To test this, in Fig. 10 we show the resulting distribution of $\langle \langle B_r^2 \rangle_{\varphi_m} \rangle_{\varphi}$ with dotted lines and the results of the full force-free simulation with solid lines. The agreement is excellent at all inclination angles: the differences are generally small and are noticeable mostly at small values of α . For instance, at $\alpha = 30^\circ$, the approximation smoothes out the otherwise well-defined equatorial peak in $\langle B_r^2 \rangle_{\varphi}$.

Since most of the spindown emerges near the equatorial plane — and these regions are rather well-described by this approximation — we expect that it provides a decent description of pulsar spindown. However, there are two difficulties in using this description in practice. First, it requires knowing the shapes plotted in Fig. 8 for all inclination angles. Second, it ignores the presence of the equatorial current sheet: in fact, the averaging in φ_m “washes out” the jump in the magnetic field across the current sheet, which is clearly seen as a jump in B_r in the bottom right of Fig. 6(b),(c). Since the current sheet could be an important location at which dissipation takes place and magnetospheric radio and gamma-ray emission is produced, we will try to find a solution that properly describes the current sheet.

6 SEMI-ANALYTICAL SOLUTION TO THE PULSAR WIND

The current sheet structure in the force-free solutions is seen more clearly in Fig. 11, which shows the view of the solution down the y -axis. The current sheet is clearly seen as the sharp stripe across the solution. Apart from a small-scale deformations, the current sheet appears to lie in a single plane inclined relative to the x - y plane.

A common description of the magnetospheric current sheet is due to Bogovalov (1999) split-monopole model. This approach gives a 3D, analytic description of the magnetospheric current sheet location under the assumption that the sheet is “painted” on the magnetosphere and is passively advected outward at the speed of light, as shown in Fig. 12. This model is in rather good agreement with the numerical simulation shown in Fig. 11 and captures both the inclination and the phase of the current sheet correctly. However, the split-monopole model assumes a piece-wise constant B_r outside of the current sheet, and this is clearly not the case in the numerical simulations.

Our goal is to construct an approximate analytic description of the 3D pulsar wind that would correctly reproduce both the location of the current sheet and the smooth variation of the magnetic field everywhere else. In particular, the solution needs to capture the gradual decrease of the jump in magnetic field strength across the current sheet as the inclination angle increases from $\alpha = 30^\circ$ to 90° , as seen in Fig. 11(b)–(d). This might seem like an intractable problem. However, as we discussed in §2, the situation is substantially simplified by the fact that to describe the entire wind solution it suffices to specify just one function, $B_r = B_r^0(\theta, \varphi)$, at a sufficiently large radius $r_0 \gg R_{LC}$ at which the lateral structure of the solution “freezes out”. After this, the rest of the solution can be

unambiguously reconstructed. As in the split-monopole model pulsar wind (Bogovalov 1999), this distribution rotates at an angular frequency Ω of the star in the φ -direction and “flies out” at essentially the speed of light in the r -direction. The full time-dependent solution combines both of these effects:

$$B_r = B_r^0(\alpha, \theta, \varphi + \Delta\varphi) \left(\frac{r}{r_0} \right)^{-2}, \quad (19)$$

where the phase shift is $\Delta\varphi = \Omega \cdot [(r - r_0)/c - (t - t_0)]$, and we approximate $B_\theta = 0$, as the wind is mostly radial at large distances (see Figs. 2 and 4). Then, the toroidal magnetic field is given by the winding of this radial field eq. (6) (see also Gruzinov 2006). Within the approximation $B_\varphi = -E_\theta$ that we will adopt, the Lorentz factor of the flow is

$$\gamma = \frac{B}{(B^2 - E^2)^{1/2}} = \frac{B}{B_r} = (1 + \Omega^2 r^2 \sin^2 \theta)^{1/2} \approx \Omega r \sin \theta / c \quad (20)$$

(Tchekhovskoy et al. 2008). In the simulations, we find that $B_\varphi^2 - E_\theta^2 \lesssim B_r^2 \ll B_\varphi^2, E_\theta^2$, so the Lorentz factor could be higher or lower by a factor $\lesssim 2$ than the estimate (20). For simplicity, we will neglect this effect.

Our goal is to construct an appropriate 2D function, $B_r^0(\theta, \varphi)$, that would satisfy the above requirements. As we discussed in §5, the structure of the pulsar wind is relatively simple in the two limiting cases:

- (i) aligned rotator ($\alpha = 0^\circ$). While no analytic solution is known, we can write down a simple analytic fitting function, eq. (18), for the numerical solution. We will denote this solution, rotated by an angle α around the y -axis, via $B_r^{(1)}(r, \alpha, \theta, \varphi) \equiv B_r^{(1)}[r, \theta_m(\alpha, \theta, \varphi), \varphi]$, where $B_r^{(1)}(r, \theta, \varphi)$ is given by eq. (18) and $\theta_m(\alpha, \theta, \varphi)$ by eq (11).
- (ii) orthogonal rotator ($\alpha = 90^\circ$), whose B_r distribution is well-described by eq. (15). We will denote this solution as $B_r^{(2)}(r, \theta, \varphi)$.

Our goal is to describe what happens in between these two limiting cases. We established that the position of the current sheet is well-described by the split-monopole model, i.e. the current sheet lies in the plane that passes through the y -axis and makes an angle α , i.e. the inclination angle, with the x - y plane. We can incorporate this feature by tilting the solution for the aligned rotator by the inclination angle, α , as described in item (i).

This is clearly not the whole story since this would lead to the magnetic peak located at $\theta_{\max} = \alpha$ in the x - z plane. However, we saw that the position of the magnetic peak is systematically shifted toward the equatorial plane, i.e., $\theta_{\max} > \alpha$. Further, the strength of the jump across the current sheet progressively decreases with increasing α . Eventually, for $\alpha = 90^\circ$, the solution becomes the orthogonal solution [see item (ii)] without any current sheet.

On a phenomenological level, this suggests that it would be advantageous to mix the tilted solution (i) with the orthogonal one (ii). This might work because the magnetic peak of the orthogonal rotator is always located at the midplane and will bias the sum to peak toward the midplane:

$$B_r^0(\alpha, \theta, \varphi) = \left[w_1(\alpha) B_r^{(1)}(\alpha, \theta, \varphi) + w_2(\alpha) B_r^{(2)}(r, \theta, \varphi - \varphi_{\max}) \right] \psi(\alpha), \quad (21)$$

where $\psi(\alpha)$ describes the variation of total open flux vs the inclination angle, as seen in Fig. 3. Here $\varphi_{\max} = 30^\circ$ is the approximate azimuth of the magnetic peak, as seen in Fig. 7. We can determine the weights w_1, w_2 , and ψ in the following way. Since the orthogonal solution (ii) vanishes at the rotational pole, i.e., $B_r^{(1)}(\theta = 0, \varphi) = B_r^{(1)}(\theta = \pi, \varphi) = 0$, we choose the value of w_2

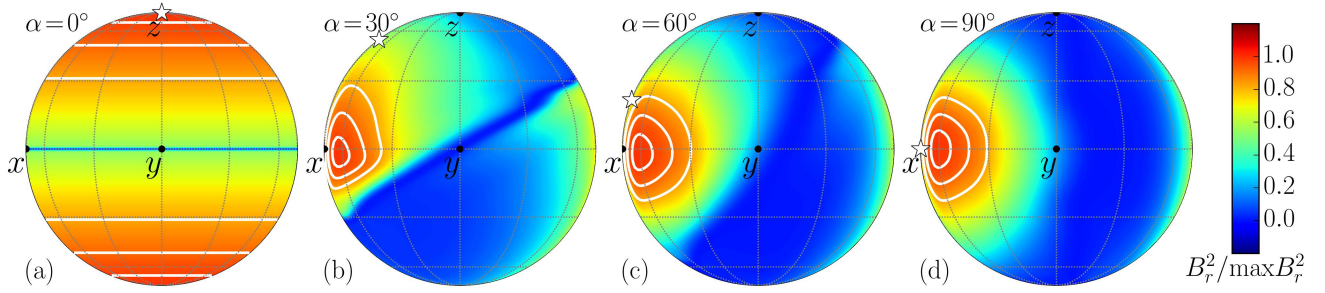


Figure 11. Colour-coded surface distribution of B_r^2 in the numerical force-free solution at $r = 6R_{LC}$ viewed down the y -axis. This is similar to Fig. 6 where the same solution is viewed down the magnetic peak. For all inclination angles, except $\alpha = 90^\circ$, the solution shows a well-defined current sheet whose orientation is well-described by the split-monopole model shown in Fig. 12.

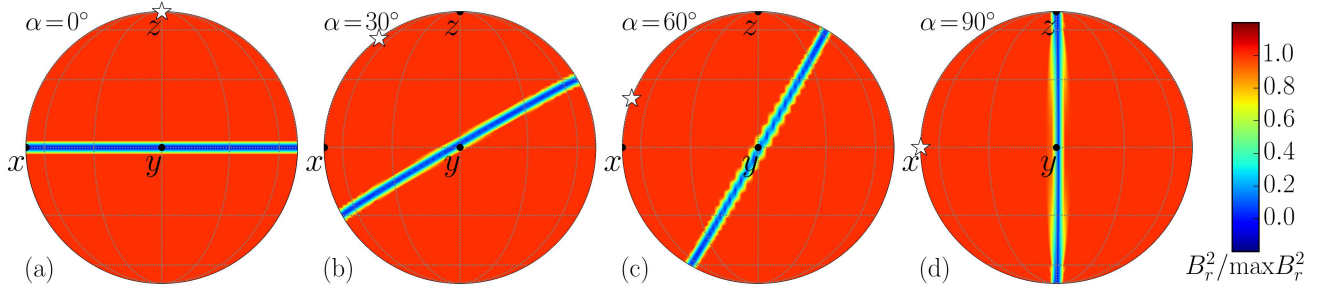


Figure 12. Colour-coded surface distribution of B_r^2 in the split-monopole solution (Bogovalov 1999). The current sheet, in which the radial magnetic field vanishes, describes the orientation of the current sheet in the numerical force-free solutions shown in Fig. 6.

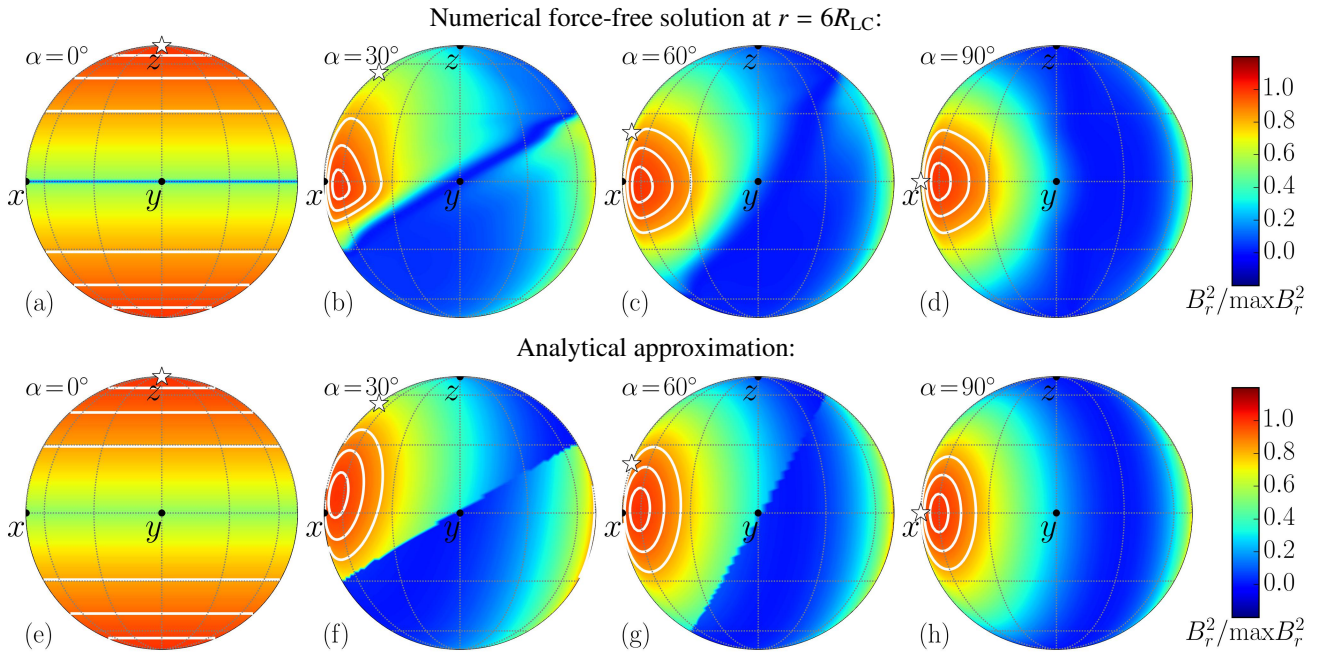


Figure 13. Colour-coded surface distribution of B_r^2 in the numerical (panels a-d) and analytical (panels e-h) solutions. For convenience of comparison, the top row of panels duplicates the numerical solution shown in Fig. 11. The analytical solution, shown in the bottom row of panels, clearly reproduces the main features of the numerical solution for all inclination angles. Firstly, the position of the current sheet (the jump in the magnitude of B_r^2) are in good agreement. Secondly, the position and size of the peaks in B_r^2 are consistent with each other to within the middle (96th percentile) contour level. Thus, the analytical approximation provides an excellent description of the numerical solution.

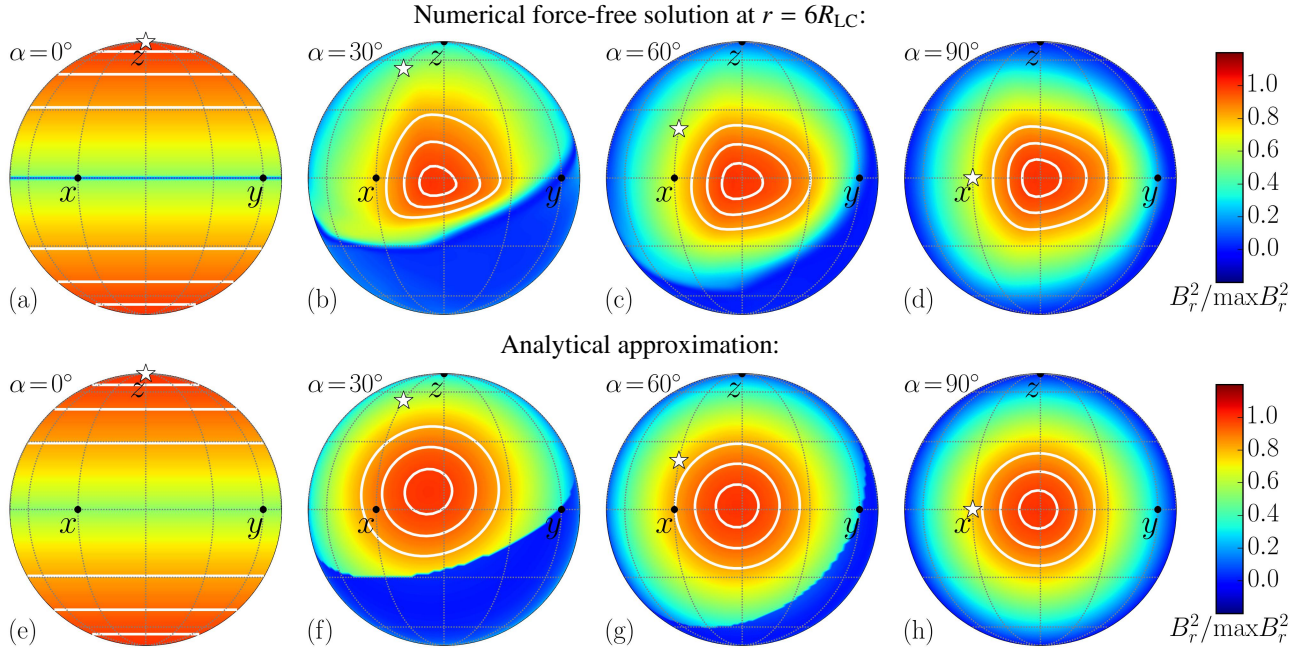


Figure 14. Same as in Fig. 13 but centred at the position of the magnetic peak. The analytic model, shown in panels (a)–(d) provides an accurate description of the numerical solution at all inclination angles.

by requiring that we get the polar value of B_r from the simulation. Next, we choose w_2 such that the weighted sum of the two solutions in the square brackets in eq. (21) gives us an inclination-independent value of the total magnetic flux. Then, we choose ψ to reproduce the dependence of the open magnetic flux on the inclination angle, as seen in the simulations and in Fig. 3. This way we find the weights of the aligned and orthogonal components of the full solution, respectively,

$$w_1(\alpha) = |1 - 2\alpha/\pi|, \quad (22)$$

$$w_2(\alpha) = 1 + 0.17|\sin 2\alpha| - w_1, \quad (23)$$

and the overall normalisation factor that accounts for the variation of the open magnetic flux with the inclination angle,

$$\psi(\alpha) = 1 + 0.2 \sin^2 \alpha. \quad (24)$$

We have found that eq. (21) with the weights given by eqs. (22)–(24) provide a good description of the numerical simulation results. We discuss the resulting two-component solution below.

Figs. 13 and 14 show the comparison of such a two-component approximation to the numerical solution from two viewing angles: one along the y -axis and the other along the magnetic peak, respectively. Fig. 13 shows that our analytic description accurately reproduces not only the position of the magnetospheric current sheet but also the magnitude of the jump in B_r^2 across the magnetospheric current sheet. This highlights an important difference from the Bogovalov (1999) split-monopole solution, in which B_r changes sign across the current sheet but maintains the same absolute magnitude, i.e., there is no jump in B_r^2 across the current sheet (see Fig. 12).

Fig. 14 shows that our analytic approximation is in excellent agreement with the numerical simulation outside of the current sheet region. In particular, for all inclination angles we considered, the analytic description captures the angular size of the magnetic peak and its location (to within 4% in B_r^2).

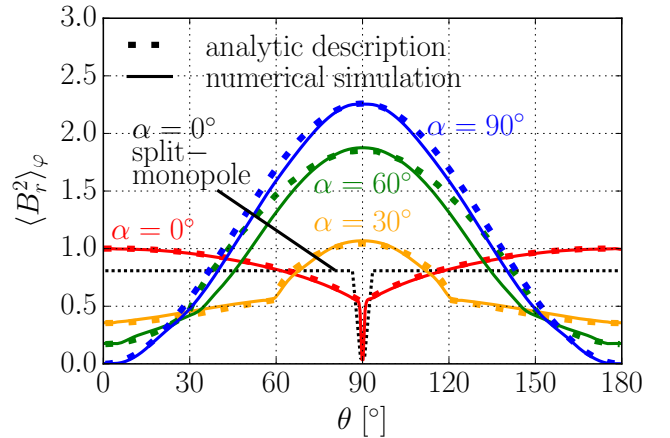


Figure 15. Angular distribution of the $\langle B_r^2 \rangle_\phi$ of the numerical force-free solution evaluated at $r = 6R_{\text{LC}}$ (solid curves) and our semi-analytical description (thick dotted curves), for different obliquities: $\alpha = 0, 30, 60,$ and 90° , shown with red, orange, green, and blue lines, respectively. Black thin dotted line shows the aligned split-monopole solution. The split-monopole solution is at the same magnetic flux as the $\alpha = 0^\circ$ aligned force-free solution, shown with the red lines. Clearly, solutions at all inclination angles show a substantial degree of non-uniformity in B_r^2 that is not present in the split-monopole solution.

Fig. 15 shows that our analytic approximation accurately describes the azimuthally-averaged radial magnetic field distribution, which sets the spindown power according to eq. (8). Importantly, it describes the magnetospheric structure not only for aligned and orthogonal rotators (by construction), but also for intermediate inclination angles. For instance, for $\alpha = 30^\circ$, it accurately captures both the low-latitude hump as well as the high-latitude wings in $\langle B_r^2 \rangle_\phi$. Similarly, the solution provides a rather good description of the pulsar wind at $\alpha = 60^\circ$, for which it only slightly over-

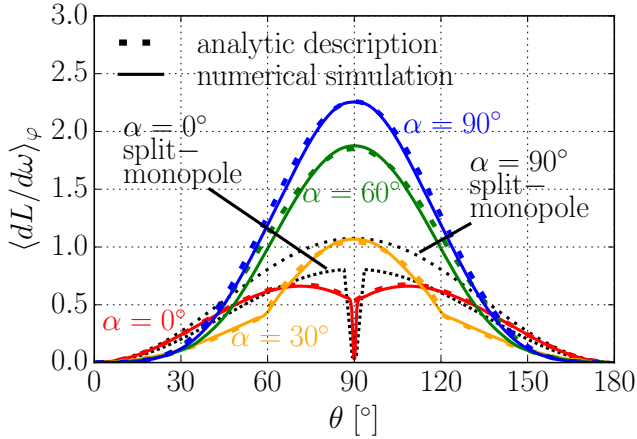


Figure 16. Angular distribution of the $\langle dL/d\omega \rangle_\varphi$ (in arbitrary units) of the numerical force-free solution (solid curves) and our semi-analytical description (thick dotted curves) for different obliquities. Fine dotted black curve shows the luminosity due to an aligned split-monopole solution and rare dotted black curve shows the luminosity due to an orthogonal split-monopole solution. The orthogonal numerical solution has a much more pronounced peak, and the peak luminosity exceeds that of the split-monopole solution by a factor of 2. This highlights the importance of accounting for the effects of non-uniformity of pulsar wind on the wind luminosity and its angular distribution.

predicts (by $\sim 5^\circ$) the width of the magnetic peak. Note that the solutions at all inclination angles are qualitatively different from the split-monopole solution, which does not have any non-uniformity in θ . For the aligned rotator, this difference emerges from the return current present in the magnetosphere: the return current, which is not included as part of the split-monopole solution, causes an additional $\vec{j} \times \vec{B}$ force, which is directed away from the midplane, and which is compensated by the magnetic pressure gradient force, which is caused by a non-uniformity in B_r and directed toward the midplane (see Appendix A).

What kind of electromagnetic luminosity does our analytic approximation imply? How does it compare with the simulated result? Fig. 16 shows the distribution of luminosity per unit solid angle, $\langle dL/d\omega \rangle_\varphi \propto \langle B_r^2 \rangle_\varphi \sin^2 \theta$ (see eq. 9), as a function of the polar angle. The black dotted line shows the expected angular distribution for a split-monopole model of Bogovalov (1999), $dL/d\omega \propto \sin^2 \theta$. Whereas this dependence is broadly representative of the aligned force-free simulation result, which we show with the red solid line, it over-predicts the luminosity in the equatorial region by as much as 50% at the expense of under-predicting the luminosity at other angles. For other inclination angles, the split-monopole solution under-predicts the luminosity by as much as a factor of 2. For instance, for $\alpha = 90^\circ$, the split-monopole solution gives the peak value of $\langle dL/d\omega \rangle_\varphi \approx 1$, much smaller than the simulated peak value is ≈ 2.25 . This is despite the open magnetic flux is the same in the split-monopole solution as in the numerical simulation. As we discussed previously, this excess spindown luminosity in oblique rotators is due to the bunching of magnetic field lines toward low-latitude regions (see §3).

7 DISCUSSION AND CONCLUSIONS

In this work, we analysed the results of 3D, time-dependent numerical simulations of oblique, plasma-filled pulsar magnetospheres

in the MHD and force-free approximations. Oblique plasma-filled pulsars spin down twice as fast as aligned pulsars (Spitkovsky 2006), i.e., the spindown luminosity L varies with the inclination angle α as

$$L \approx L_{\text{aligned}}(1 + \sin^2 \alpha). \quad (25)$$

The reasons for such an increase are not understood. Could this increase be caused by the changes in the amount of open magnetic flux? Only to a degree: we found that changes in the open magnetic flux account for about 40% of the increase. We argue that the other 60% of the increase is due to a *nonuniform bunching of magnetic field lines toward the equatorial plane*. This redistribution allows the field lines to extract the rotational energy more efficiently, thereby accounting for the rest of the increase in the spindown luminosity.

To illustrate this effect, we constructed a toy model, in which we approximated the angular distribution of the radial magnetic field, B_r , by that of a dipole. Dipole magnetic field strength peaks at the magnetic poles. As this field distribution rotates with the star, the magnetic field lines become wound up around the axis. The faster the winding of a field line, the more that field line contributes to the spindown. Since the winding is slowest at the magnetic poles (there $v_\varphi = 0$) and fastest at the equator (v_φ is maximum), the field lines near the polar magnetic peak do not contribute much to the spindown. However, in an inclined rotator, the dipolar peak moves closer to the equatorial plane. The field lines near the inclined peak contribute to the stellar spindown more efficiently and lead to an increase in the spindown of an oblique rotator relative to the aligned rotator. We showed that the spindown luminosity in this simple model follows the dependence given in eq. (25), which illustrates the importance of magnetic field bunching on the spindown luminosity.

The magnetic field of an actual pulsar is not dipolar. Is there a quantitative way of describing the non-uniformity of magnetic field in the pulsar wind? The good news is that it is sufficient to prescribe a single function – a distribution of B_r on a sphere of a sufficiently large radius – in order to fully recover the asymptotic, 3D structure of a pulsar wind. In particular, for an aligned rotator, the distribution of B_r is axisymmetric, and we parametrised it via a single scalar function (see eq. 18).

At first glance, the structure of oblique rotators appears to be much more complicated than that of the aligned one. The good news is that an orthogonal force-free rotator exhibits a rather featureless and simple radial magnetic field distribution, $B_r \propto \sin \theta \cos \varphi$, i.e., the same as of the vacuum dipole that is put on its side (see eq. 15)!

Now, with these two solutions for the asymptotic pulsar wind – for the aligned and orthogonal plasma-filled rotators – at hand, we combined them into an approximate, two-component solution that describes the simulation results at all inclination angles (§6).

That the full solution is a combination of the two components is particularly interesting for the following reason. The magnetic field in the aligned component of the solution undergoes a jump in the equatorial plane. However, the field remains smooth in the orthogonal component. This means that the relative weights with which the two solutions enter the full solution tell us about the strength of the jump in magnetic field strength and therefore the *strength of the magnetospheric current sheet*.

As the inclination angle increases, the contribution of the aligned solution gradually decreases (eq. 22) and the magnetospheric current sheet weakens, i.e., the jump across the sheet in the magnetic field decreases. The current sheet completely disappears

for a force-free orthogonal rotator, as seen in Fig. 13(d),(h). This suggests that the amount of dissipation in near-orthogonal pulsar magnetospheres might be *qualitatively* smaller than at intermediate obliquities. This might be the reason for lower dissipation in the current sheets found in global PIC simulations (Philippov et al. 2014). However, the absence of a jump in the magnetic field in a force-free solution does not mean that the dissipation is entirely absent, as found in both recent 3D MHD (Tchekhovskoy et al. 2013) and PIC (Philippov et al. 2014) simulations of oblique pulsar magnetospheres.

Whereas force-free and MHD simulations do not include the microphysics of the magnetospheric current sheets and reconnection, they are extremely useful because they can be extended to extremely large distances and give us the full, nonlinear structure of the pulsar wind electromagnetic field that is otherwise difficult to obtain. In particular, they offer us a unique opportunity to determine the smooth structure of the solution outside of the current sheets and compute the spindown luminosity, its angular distribution, and its dependence on the obliquity angle of the pulsar. For instance, we find that the current sheets in our analytic description of the pulsar wind are quite unusual in that the magnitude of $|B_r|$ undergoes a substantial jump across the sheet. Since asymptotically in the pulsar wind the total (radial plus toroidal) lab-frame magnetic pressure is tightly related to square of the radial magnetic, B_r^2 , via $B^2/8\pi = (B_r^2 + B_\phi^2)/8\pi \approx B_r^2(1 + \Omega^2 r^2 \sin^2 \theta/c^2)/8\pi$ (see eq. 6), the lab-frame magnetic pressure also undergoes a jump across the magnetospheric current sheet.

However, having such a jump is at odds with the expectation that the total pressure (which is dominated by magnetic pressure outside the sheets), must be the same on both sides of the sheet: otherwise, the current sheet would be pushed to the side with a lower pressure until the two pressures came to an equilibrium. There is a flaw in this argument: since our simulations are relativistic, we need to measure the magnetic pressure in the *fluid* frame, which is different than the pressure in the *lab* frame because the pulsar wind flows outward at a relativistic velocity, with a Lorentz factor $\gamma \gg 1$ relative to the star. Hence, it is the fluid-frame magnetic pressure, $p_{\text{mag}} \equiv b^2/8\pi \equiv B^2/8\pi\gamma^2$, that is continuous across the current sheet. How can this happen if the lab-frame magnetic pressure is discontinuous? This can occur if the fluid elements on the two sides of the current sheet move at *substantially different Lorentz factors*, $\gamma_1 \neq \gamma_2$, such that even though the lab-frame magnetic pressures are different, $B_1^2/8\pi \neq B_2^2/8\pi$, the fluid-frame magnetic pressures are the same, $B_1^2/8\pi\gamma_1^2 \equiv b_1^2/8\pi \approx b_2^2/8\pi \equiv B_2^2/8\pi\gamma_2^2$.

Thus, that the square of the radial magnetic field, B_r^2 , undergoes a substantial jump, which we find both in our force-free and MHD simulations of oblique pulsar magnetospheres as well as in our analytic model, necessarily implies that the fluid elements on the two sides of the current sheet *move at a relativistic velocity relative to each other*. This relative motion is independent of the internal physics of the current sheet and is a generic feature of the large-scale geometry, or topology, of the pulsar magnetosphere. This might be interpreted as follows: the reconnection in the current sheet is a type of *driven*, rather than spontaneous, reconnection. Thus, in order to accurately predict the properties of current sheet reconnection rate, particle acceleration, and emission, local simulations of reconnection need to be constructed for the specific geometry and type of discontinuity across the current sheet in order to properly reflect the driving exerted on the current sheet by the global magnetospheric structure (Sironi & Spitkovsky 2014; Guo et al. 2014). In particular, local simulations of *driven* reconnection

are needed to properly represent the magnetospheric current sheet physics.

Our analytic description of the pulsar magnetosphere provides a 3D electromagnetic structure of a pulsar wind near and beyond the light cylinder for both aligned and oblique pulsars. This is useful for constructing the models of emission from the magnetospheric current sheet and modelling pulsar gamma-ray light curves (Arka & Dubus 2013; Uzdensky & Spitkovsky 2014). The nonuniformity of the pulsar wind and the deviations of lateral structure from the split-monopole expectation can be included into and will improve the accuracy of the models of pulsar wind nebulae (Camus et al. 2009; Porth et al. 2014a,b), supernovae remnants, and magnetar-powered supernovae (Woosley 2010; Kasen & Bildsten 2010) and core-collapse gamma-ray bursts (Metzger et al. 2011). For all of these systems, if an oblique rotator is a generic situation, the emerging outflow shows smooth, sinusoidal-like variations (e.g., see Fig. 14) separated by jumps at the current sheets. Because of these variations, the energy flux is more strongly concentrated toward the edges of the emerging outflow than in the standard split-monopole approximation for the pulsar wind.

In the magnetar model of core-collapse gamma-ray bursts, a pulsar wind focuses into a pair of tightly collimated jets. If jet emission correlates with its power (Nemmen et al. 2012), variability of the pulsar wind could translate into periodic gamma-ray variability that is directly observable. In the particularly clean case of an orthogonal rotator, the emerging pulsar wind shows smooth sinusoidal-like variation at the rotational period of the neutron star that could lead to sinusoidal-like modulation of the high-energy emission. That this signature is not routinely seen in the light curves of long-duration gamma-ray bursts suggests several possibilities. The central compact object could be a black hole or a (nearly) aligned rotator and produce no periodic variability. If the central object is an oblique rotator, the absence of such variability might be suggestive of an emission mechanism that washes out small time-scale variability of the central engine. For instance, in subphotospheric gamma-ray emission models (e.g., Giannios 2006, 2008; Pe'er et al. 2006; Giannios & Spruit 2007; Beloborodov 2010, 2013), the emission is formed over a wide range of radii, which means that the emission is sensitive only to large-scale jet structure. How gamma-ray burst emission is produced by inhomogeneous jets warrants further investigation.

ACKNOWLEDGEMENTS

We thank Jon Arons and Vasily Beskin for insightful discussions. AT was supported by NASA through Einstein Postdoctoral Fellowship grant number PF3-140115 awarded by the Chandra X-ray Center, which is operated by the Smithsonian Astrophysical Observatory for NASA under contract NAS8-03060, and NASA via High-End Computing (HEC) Program through the NASA Advanced Supercomputing (NAS) Division at Ames Research Center that provided access to the Pleiades supercomputer, as well as NSF through an XSEDE computational time allocation TG-AST100040 on NICS Kraken, Nautilus, TACC Stampede, Maverick, and Ranch. This work was supported in part by NASA grant NNX14AQ67G and Simons Foundation (grant 267233 to AS). We used Enthought Canopy Python distribution to generate figures for this work.

APPENDIX A: ANGULAR DISTRIBUTION OF THE POLOIDAL FIELD IN THE ALIGNED PULSAR MAGNETOSPHERE

In this section we show that the angular structure of B_r in the aligned case can be explained analytically. The force balance equation in the axisymmetric steady state can be rewritten as (Tchekhovskoy et al. 2008)

$$\frac{B_p^2 - E^2}{4\pi R_c} - (\mathbf{R} \cdot \mathbf{n}) \frac{B_\phi^2 - E^2}{4\pi R} - \frac{\partial}{\partial \mathbf{n}} \left(\frac{B^2 - E^2}{8\pi} \right) = 0, \quad (\text{A1})$$

where R_c is the curvature of poloidal field lines, \mathbf{R} is cylindrical radius, and \mathbf{n} is the unit vector along the local electric field. At large distances from the pulsar the poloidal magnetic field is mostly radial, so $\frac{\partial}{\partial \mathbf{n}} \approx -\frac{1}{r} \frac{\partial}{\partial \theta}$ and $\mathbf{R} \cdot \mathbf{n} \approx -\cos \theta$. With this we can rewrite the force balance as

$$-\frac{B_p^2 - E^2}{4\pi R_c} - \cos \theta \frac{B_\phi^2 - E^2}{4\pi R} - \frac{1}{r} \frac{\partial}{\partial \theta} \left(\frac{B^2 - E^2}{8\pi} \right) = 0. \quad (\text{A2})$$

We will evaluate this equation just above the equator, thus neglecting all terms containing $\cos \theta$, and $R = r \sin \theta \approx r$. The last term in (A2) can be rewritten as

$$B^2 - E^2 = \frac{4I^2}{c^2 r^2 \sin^2 \theta} + B_p^2 (1 - \Omega^2 r^2 \sin^2 \theta / c^2), \quad (\text{A3})$$

where we used the MHD condition $E^2 = \Omega^2 R^2 B_p^2 / c^2$, and the Ampere's law, which provides the relation between the toroidal field and the enclosed current $I(r, \theta) B_\phi = 2I / cR$.

$$-B_p^2 \frac{1 - R^2 / R_{LC}^2}{4\pi R_c} - \frac{8}{c^2 R^3} I \frac{dI}{d\theta} = \frac{1 - R^2 / R_{LC}^2}{R} \frac{\partial B_p^2}{\partial \theta}. \quad (\text{A4})$$

Finally, in the wind region $R \gg R_{LC}$ we get

$$\frac{\partial B_p^2}{\partial \theta} = \frac{8R_{LC}^2}{c^2 R^4} I \frac{dI}{d\theta} - B_p^2 \frac{R}{4\pi R_c}. \quad (\text{A5})$$

We find that the first term dominates at $R > 2R_{LC}$ and is negative just above the equator because of the presence of the volume-distributed return current. Finally, we obtain $\frac{\partial B_p^2}{\partial \theta} < 0$ as it is in the simulation.

APPENDIX B: FINITE MAGNETISATION EFFECTS

Note that in many of the systems, such as in PWNe and SNRs, pulsar wind propagates for many decades in radius, so that eventually the flow becomes super-fast magnetosonic. This happens at the fast magnetosonic surface, at which the flow reaches Lorentz factor $\gamma_F \approx \gamma_{\max}^{1/3}$, where γ_{\max} is the terminal Lorentz factor that the outflow would achieve if all of its electromagnetic energy were converted into kinetic energy flux (Beskin et al. 1998; Tchekhovskoy et al. 2009). For pulsars, theoretical estimates suggest $\gamma_{\max} \sim 10^4 - 10^6$ (e.g., Kennel & Coroniti 1984a,b). Since in a force-free flow the Lorentz factor increases approximately linearly with distance from the star, $\gamma \approx r \sin \theta / R_{LC}$, it crosses the fast surface at $r_F \sim \mu^{1/3} R_{LC} \sim (20 - 100) R_{LC}$. Beyond this distance, $\gamma \sim \mu^{1/3} \ln^{1/3}(r/r_F)$ (see Appendix B in Tchekhovskoy et al. 2009). The fast surface is located at a very short distance compared to those of interest in PWNe and SNRs, which means that finite-magnetisation, MHD effects will set in long before the pulsar wind starts to radiate due to the interaction with the ambient medium in these astrophysical systems. Will this lead to large deviations away from the force-free structure that we have considered? We are interested in the field lines that make a

small angle with the midplane, $\theta' = \pi/2 - \theta$, since it is these field lines that carry most of the energy flux. Fortunately, once the outflow accelerates up to a large Lorentz factor, it is extremely difficult to reorient it. In fact, the relative change in the direction of the flow $\Delta\theta'/\theta' = \gamma/\gamma_{\max} \sim \mu^{-2/3} \ln^{1/3}(r/r_F) \ll 1$, even for a really small $\mu \sim 10^2$ and a really large $r = 10^{10} r_F$. The only place where the finite magnetisation MHD effects might make a difference are the polar regions of the flow, which, however, are energetically unimportant.

REFERENCES

- Arka I., Dubus G., 2013, *A&A*, 550, A101
 Beloborodov A. M., 2010, *MNRAS*, 407, 1033
 Beloborodov A. M., 2013, *ApJ*, 764, 157
 Belyaev M. A., 2014, *ArXiv:1412.2819*
 Beskin V. S., 1997, *Soviet Physics Uspekhi*, 40, 659
 Beskin V. S., Gurevich A. V., Istomin Y. N., 1993, *Physics of the pulsar magnetosphere*. Cambridge University Press
 Beskin V. S., Kuznetsova I. V., Rafikov R. R., 1998, *MNRAS*, 299, 341
 Bogovalov S. V., 1999, *A&A*, 349, 1017
 Camus N. F., Komissarov S. S., Bucciantini N., Hughes P. A., 2009, *MNRAS*, 400, 1241
 Cerutti B., Philippov A., Parfrey K., Spitkovsky A., 2014, *ArXiv:1410.3757*
 Chen A. Y., Beloborodov A. M., 2014, *ApJ*, 795, L22
 Contopoulos I., Kazanas D., Fendt C., 1999, *ApJ*, 511, 351
 Deutsch A. J., 1955, *Annales d'Astrophysique*, 18, 1
 Giannios D., 2006, *A&A*, 457, 763
 Giannios D., 2008, *A&A*, 480, 305
 Giannios D., Spruit H. C., 2007, *A&A*, 469, 1
 Goldreich P., Julian W. H., 1969, *ApJ*, 157, 869
 Gruzinov A., 2005, *Physical Review Letters*, 94, 021101
 Gruzinov A., 2006, *ApJ*, 647, L119
 Guo F., Li H., Daughton W., Liu Y.-H., 2014, *Physical Review Letters*, 113, 155005
 Ingraham R. L., 1973, *ApJ*, 186, 625
 Kalapotharakos C., Contopoulos I., 2009, *A&A*, 496, 495
 Kalapotharakos C., Contopoulos I., Kazanas D., 2012, *MNRAS*, 420, 2793
 Kasen D., Bildsten L., 2010, *ApJ*, 717, 245
 Kennel C. F., Coroniti F. V., 1984a, *ApJ*, 283, 694
 Kennel C. F., Coroniti F. V., 1984b, *ApJ*, 283, 710
 Komissarov S. S., 2006, *MNRAS*, 367, 19
 McKinney J. C., 2006, *MNRAS*, 368, L30
 Mestel L., Shibata S., 1994, *MNRAS*, 271, 621
 Metzger B. D., Giannios D., Thompson T. A., Bucciantini N., Quataert E., 2011, *MNRAS*, 413, 2031
 Michel F. C., 1974, *ApJ*, 187, 585
 Nemmen R. S., Georganopoulos M., Guiriec S., Meyer E. T., Gehrels N., Sambruna R. M., 2012, *Science*, 338, 1445
 Parfrey K., Beloborodov A. M., Hui L., 2012, *MNRAS*, 423, 1416
 Pe'er A., Mészáros P., Rees M. J., 2006, *ApJ*, 642, 995
 Pétri J., 2012, *MNRAS*, 424, 605
 Philippov A. A., Spitkovsky A., 2014, *ApJ*, 785, L33
 Philippov A. A., Spitkovsky A., Cerutti B., 2014, *ArXiv:1412.0673*
 Porth O., Komissarov S. S., Keppens R., 2014a, *MNRAS*, 443, 547
 Porth O., Komissarov S. S., Keppens R., 2014b, *MNRAS*, 438, 278
 Ruiz M., Paschalidis V., Shapiro S. L., 2014, *Phys. Rev. D*, 89, 084045
 Sironi L., Spitkovsky A., 2014, *ApJ*, 783, L21
 Spitkovsky A., 2006, *ApJ*, 648, L51
 Tchekhovskoy A., McKinney J. C., Narayan R., 2008, *MNRAS*, 388, 551
 Tchekhovskoy A., McKinney J. C., Narayan R., 2009, *ApJ*, 699, 1789
 Tchekhovskoy A., Spitkovsky A., Li J. G., 2013, *MNRAS*, 435, L1
 Timokhin A. N., 2006, *MNRAS*, 368, 1055
 Uzdensky D. A., Spitkovsky A., 2014, *ApJ*, 780, 3
 Woosley S. E., 2010, *ApJ*, 719, L204